Coevolution of continental ice cover and permafrost extent over the last glacial-interglacial cycle in North America

Lev Tarasov[1] and W. R. Peltier[2]

Received 14 August 2006; revised 20 March 2007; accepted 24 April 2007; published 27 June 2007.

[1] The bed thermal characteristics of a glacial systems model that has been calibrated against a large set of relative sea level, geodetic, and strandline observations are examined for the previously glaciated sector of the North American continent. The model compares favorably against the present-day extent of permafrost and against the observed temperature profiles from three deep boreholes when appropriate bed thermal conductivities are employed. Estimates for the present-day depth field of the lower permafrost boundary are presented. We find a significant disequilibrium in the lower permafrost boundary for most of the Arctic region, with present-day depth as much as 250 m shallower than the equilibrium value for present-day climate forcing. This is largely due to the ongoing response to the loss of ice cover from the glacial period. The time evolution of the subglacial warm-based area fraction is also presented together with calibration-derived confidence intervals. A peak warm-based fraction of 50% ± 6% is obtained at Last Glacial Maximum. The timing of the three largest ice volume maxima that were produced in response to the obliquity component of orbital forcing during the last glacial cycle matches that of the maxima for the warm-based area fraction with no significant phase delay. Warm-based conditions are required to enable ice streaming (fast flow) in the model. It is therefore hypothesized that the expansion of the area covered by warm-based ice played a critical role in producing a highly dynamic ice sheet during both the most intense growth and recession phases.

Citation: Tarasov, L., and W. R. Peltier (2007), Coevolution of continental ice cover and permafrost extent over the last glacial-interglacial cycle in North America, *J. Geophys. Res.*, *112*, F02S08, doi:10.1029/2006JF000661.

1. Introduction

[2] The present-day three-dimensional bed thermal field and related depth distribution of permafrost over the polar continents reflects the history of ground surface thermodynamic forcing. Over most of the landmass of Canada, this forcing was often decoupled from the regional climate by the presence of glacial ice. The impact of this decoupling is, however, poorly constrained, in part because of the limited number of direct measurements resulting from the general inaccessibility of the regions where permafrost presently exists. The present and future depth of permafrost throughout Arctic Canada together with the associated subsurface temperature regime are therefore likewise poorly constrained. In order to accurately predict the expected impact of ongoing global warming on permafrost degradation, we require a model that is demonstrably able to explain its past evolution and present state.

[3] Past studies of long-term permafrost evolution have traditionally been site-specific with poorly constrained and highly simplified climate forcings and with no consideration of surface ice cover [e.g., *Osterkamp and Gosink*, 1991]. Model-based analyses employing three-dimensional thermomechanically coupled ice sheet models and constrained climate chronologies offer a route for analyzing and predicting past and present subsurface temperature fields and thus permafrost depth. Although there have been a few model studies that have examined the evolution of ice sheets across the North American continent [e.g., *Tarasov and Peltier*, 1999; *Marshall et al.*, 2000; *Marshall and Clark*, 2002; *Bauder et al.*, 2005], the resultant ice sheet chronologies have been poorly constrained because of poorly understood climate forcings, limitations in the representation of fast flow and ice calving dynamics, and the lack of data/model integration. This is all too evident in the fact that meaningful error bars are essentially never attached to model-based inferences in the glaciological modeling field. Furthermore, though one past study has considered subglacial ground surface permafrost evolution under the southern Laurentide ice sheet [*Bauder et al.*, 2005], none have considered the evolution of the three-dimensional bed thermal (and associated permafrost depth) field. Accordingly, no previous analyses employing glaciological models have

[1]Department of Physics and Physical Oceanography, Memorial University of Newfoundland, St. John's, Newfoundland, Canada.
[2]Department of Physics, University of Toronto, Toronto, Ontario, Canada.

Copyright 2007 by the American Geophysical Union.
0148-0227/07/2006JF000661

Table 1. Model Parameters

Definition	Parameter	Value
Lithospheric thickness	L_e	100 km
Latent heat of fusion	L	3.35×10^5 J kg^{-1}
Ice density	ρ_i	910 kg m^{-3}
Ice specific heat capacity	$c_i(T)$	$(152.5 + 7.122\ T)$ J kg^{-1} K^{-1}
Ice thermal conductivity	$k_i(T)$	$9.828 \cdot \exp(-0.0057 \cdot T)$ W m^{-1} K^{-1}
Bedrock density	ρ_b	3300 kg m^{-3}
Bedrock specific heat capacity	C_r	1000 J kg^{-1} °C $^{-1}$
Bedrock thermal conductivity	k_b	3 W m^{-1} K^{-1} °C $^{-1}$
Standard deviation, PDD model	σ	5.2°C
Standard deviation, accumulation model	σ_p	$\sigma - 1$ °C
Number of ice thermodynamic levels	nz_i	65
Number of bed thermodynamic levels	nz_b	20
Longitudinal ISM grid resolution	$\Delta\phi$	1.0°
Latitudinal ISM grid resolution	$\Delta\theta$	0.5°
Glen flow law constant, $T < -10$°C	B_{gc}	1.14×10^{-5} Pa^3 yr^{-1}
Glen flow law constant, $T > -10°$ C	B_{gw}	5.47×10^{10} Pa^3 yr^{-1}
Flow law enhancement factor	E	4.0
Creep activation energy of ice, $T < -10$°C	Q_c	6×10^4 J mol^{-1}
Creep activation energy of ice, $T > -10$°C	Q_c	1.39×10^5 J mol^{-1}
Glen flow law exponent	n	3
TTOP ground parameter	A_{ts}	0.583269
TTOP ground parameter	B_{ts}	0.0286538
TTOP ground parameter	A_{tr}	0.72829
TTOP ground parameter	B_{tr}	0.0278275

taken into account the significant thermal offsets for ice-free ground temperature forcing due to seasonal snow cover and to the difference between thawed and frozen ground thermal conductivities [*Smith and Riseborough*, 2002]. The lack of comparisons between model results and observed permafrost extent, depth, and borehole temperature profiles leaves the validity of bed thermal results from glaciological modeling unclear.

[4] The depth and spatial extent of permafrost over time has important implications for subglacial and periglacial landform development, subglacial hydrology, and the evolution of ice sheets. Past studies [e.g., *Clark*, 1994; *Licciardi et al.*, 1998; *Tarasov and Peltier*, 2004] have shown that fast ice flow processes have played a critical role in the evolution of the North American ice sheet complex. Fast ice flow due to basal decoupling generally requires warm basal conditions. However, fast flow over sediment also depends on adequate basal water pressure for which permafrost could play an important role in impeding subglacial drainage. On the basis of ensemble results with a glaciological model, *Marshall and Clark* [2002] have concluded that only 20%–40% of the Laurentide Ice Sheet was warm based at Last Glacial Maximum (LGM) with a much higher fraction during deglaciation. On this basis, they suggest that the transition to widespread warm-based subglacial conditions played a critical role in glacial terminations. However, the ensemble employed in their analysis was subject to limited constraint as evidenced by the approximately 100 m eustatic equivalent sea level fall at LGM for the model run for which detailed chronologies were provided. Such a large sea level contribution would leave little more than a total 20 m eustatic rise to be accounted for from the remaining ice sheets [*Peltier and Fairbanks*, 2006]. This remainder is half of that inferred by the ICE-5G reconstruction [*Peltier*, 2004] on the basis of the inversion of relative sea level (RSL) data. A reexamination of this previous result is therefore in order.

[5] Here we use a glacial systems model (GSM) that is much more highly constrained than models employed in previous studies to consider the following questions concerning the evolution of basal temperature and permafrost fields for the regions of North America that were subject to glaciation over the last ice age cycle. First, what is the present-day permafrost depth field and what are the associated error bars? Secondly, what is the present-day disequilibrium in the permafrost depth field? Finally, what impact has the evolution of ice cover and climate over the last ice age cycle had on the bed thermal and permafrost fields? Comparisons of model predictions against present-day observations are also presented to further test and validate our model results.

2. Description of Model Components

[6] The core of the Memorial University of Newfoundland/University of Toronto Glacial Systems Model (GSM) is a three-dimensional thermomechanically coupled ice sheet model (ISM) (including bed thermodynamics) asynchronously coupled to a viscoelastic model of the glacial isostatic adjustment process. As the model has been described in detail previously [*Tarasov and Peltier*, 1999, 2004], only an abbreviated description is provided herein. Model parameters are summarized in Table 1.

2.1. Thermomechanical Ice Sheet Model

[7] The base thermomechanically coupled model is that originally described by *Tarasov and Peltier* [1999] with more recent improvements discussed by *Tarasov and Peltier* [2002]. Ice flow is determined by solving the vertically integrated form of the equation for the conservation of mass:

$$\frac{\partial H}{\partial t} = -\nabla_h \cdot \int_{z_b}^{h} \vec{\mathbf{V}}(z)\, dz + G(\vec{\mathbf{r}}, T), \tag{1}$$

where H is the local ice thickness and G is the net surface and basal mass balance. The horizontal ice velocity $\vec{\mathbf{V}}(z)$ is computed using the standard Glen flow law for ice rheology with a factor 4.0 flow enhancement. The temperature dependence of the ice rheology is as per the EISMINT II intercomparison project specifications [*Payne et al.*, 2000].

[8] The ice temperature field (T) is computed on the basis of conservation of internal energy. Vertical diffusion and three-dimensional advection of heat as well as heat generated by deformation work (Q_d) are taken into account by numerical solution of the following partial differential equation for the conservation of energy:

$$\rho_i c_i(T)\frac{\partial T}{\partial t} = \frac{\partial}{\partial z}\left\{k_i(T)\frac{dT}{dz}\right\} - \rho_i c_i(T)\mathbf{V}\cdot\nabla T + Q_d. \quad (2)$$

Heat generated by basal sliding is introduced through the basal boundary condition. Ice temperature is not allowed to rise above the pressure melting point. Excess energy from this condition is applied to meltwater production. The ice surface temperature boundary condition also accounts for the latent heat of refreezing of meltwater and rain.

[9] Fast flow due to basal decoupling occurs when the basal ice approaches the pressure melting point. This condition alone allows moderately fast flows in the model due to sliding. Very fast flows are allowed with basal till deformation, which is geographically restricted in the model according to the present-day surficial sediment availability. Ice shelves have complete basal decoupling and are thus represented in the model by very strong sliding described as a linear function of the gravitational driving stress.

2.2. Bed Thermal Model

[10] The subglacial temperature field is computed at each grid point with a 1D (vertical diffusion only) bed thermal model that spans a depth of 3 km. The model is therefore defined by the following partial differential equation for energy balance:

$$\rho_b C_b \frac{\partial T}{\partial t} = k_b \frac{\partial^2 T}{\partial z^2}. \quad (3)$$

Bedrock density ρ_b is set to the mean value for the lithosphere (3300 kg m^{-3}). The values of the bed thermal conductivity k_b and effective heat capacity C_b are poorly constrained because of the dependence of these parameters on bed composition and both water and ice content. Rock thermal conductivity at 0°C ranges from 1.9 to 3.5 and 8.8 W m^{-1} K^{-1} for shale, granite, and quartz respectively, while organic matter, water and ice have thermal conductivities of 0.25, 0.56, and 2.24 W m^{-1} K^{-1} respectively [*Weast*, 1981]. A value of 3 W m^{-1} K^{-1} for k_b was chosen following the specifications for the 1997 EISMINT II model intercomparison. The effective bed heat capacity C_b includes a term accounting for the impact of latent heat of fusion L [*Osterkamp*, 1987; *Williams and Smith*, 1989; *Mottaghy and Rath*, 2006]:

$$C_b = C_r + L\frac{\partial \alpha_r}{\partial T}. \quad (4)$$

where α_r is the volumetric unfrozen water content. α_r is simply represented as a stepwise linear function with a maximum sediment porosity value of 0.3 at the pressure melting point and a null value at 2°C below the pressure melting point to maximize conservation of energy under a linear solution and ensure numerical stability. A test with a two-step piecewise linear unfrozen water function with nonzero values to −10°C that better approximates the observed exponential decline [*Williams and Smith*, 1989] produced no discernable impact on the computed borehole temperature profiles that are presented below. Nor was there a significant impact on the area of warm subglacial conditions over the last 60 ka. Sediment depth is taken from *Laske and Masters* [1997] and bedrock is assumed to be nonporous. Bedrock heat capacity C_r is set to 1000 J kg^{-1} K^{-1}, again as per the EISMINT II specifications.

[11] Boundary conditions for the bed thermal model are simply

$$\begin{aligned} T(0) &= T_{\text{ground}} \qquad \text{No ice} \\ T(0) &= T_{\text{ice}}(\text{base}) \qquad \text{Ice} \\ -k_b\,\partial_z T(3\,\text{km}) &= G_f(x,y). \end{aligned} \quad (5)$$

Unless otherwise specified, the deep geothermal heat flux $G_f(x, y)$ is taken from the digital map of *Pollack et al.* [1993]. There are significant thermal offsets at the ground surface (relative to mean annual air temperature) due to the insulating effects of seasonal snow cover [*Goodrich*, 1982; *Zhang*, 2005] and the impact of vegetation on radiative balance and snow accumulation [*Williams and Smith*, 1989] The differing thermal conductivity of frozen and thawed ground also produces an effective offset across the active layer for calculations based on mean annual values [*Romanovsky and Osterkamp*, 1995; *Smith and Riseborough*, 2002]. To account for these offsets for ice-free land, we use a quadratic parameterization for the (near surface) ground temperature (T_{ground}) as a function of mean annual air temperature (which is based on their application of Canadian climate station data for air temperature and snowfall to their TTOP (temperature at the top of permafrost) model [*Smith and Riseborough*, 2002]):

$$\begin{aligned} T_{\text{ground}} &= T_{\text{air}} - 1^\circ\text{C}, \qquad T_{\text{air}} > 4.118^\circ\text{C} \\ T_{\text{ground}} &= T_{\text{air}}, \qquad T_{\text{air}} < -17^\circ\text{C} \\ T_{\text{ground}} &= 1.2^\circ\text{C} + A_{ts} * T_{\text{air}} - B_{ts} * T_{\text{air}}^2, \qquad \text{otherwise.} \end{aligned} \quad (6)$$

The ratio of thawed to frozen ground thermal conductivities in this parameterization is assumed to be 0.6 for regions with sediment cover. It should also be noted that the regression of *Smith and Riseborough* [2002] was computed only for stations with mean annual temperatures below 5°C. We have therefore conservatively truncated the offset at −1°C for temperatures above 4.118°C.

[12] For regions that are free of surface sediment, a unit ratio of thermal conductivities is assumed, and the parameterization takes the following form:

$$\begin{aligned} T_{\text{ground}} &= T_{\text{air}}, \qquad T < -17.14^\circ\text{C or } T > 7.375^\circ\text{C} \\ T_{\text{ground}} &= 3.51751^\circ\text{C} + A_{tr} * T_{\text{air}} - B_{tr} * T_{\text{air}}^2, \qquad \text{otherwise.} \end{aligned} \quad (7)$$

Table 2. Ensemble Parameters

GSM Aspect	Number of Parameters
Fast flow dynamics	5
Ice calving	4
Margin forcing	2
Version of Eemian surface topography	1
Climate	20

Sediment free grid cells were identified according to the till map used for constraining fast flow due to till deformation with the additional constraint that the cells also have minimum values in the global sediment map of *Laske and Masters* [1997]. The main impact of this latter condition is to improve the fit to the present-day observed extent of permafrost over Quebec and Labrador.

[13] The bed thermal model is implicitly coupled to the ice thermodynamics computation. The model uses 20 vertical layers, with layer thickness increasing exponentially with depth. Permafrost depth is determined by linear interpolation between bounding grid cells to the depth of 0°C temperature relative to the pressure melting point for ice (assuming hydrostatic pressure throughout and zero pore water salinity).

2.3. Bedrock Response and RSL History Determination

[14] The computation of the viscoelastic bedrock response to the changing surface load follows a linear field theory for a spherically symmetric Maxwell model of the Earth [*Peltier*, 1974, 1976]. We use the VM2 Earth rheology [*Peltier*, 1996; *Peltier and Jiang*, 1996] with a 100 km thick lithosphere. The PREM model [*Dziewonski and Anderson*, 1981] provides the radial elastic structure. The bedrock response is asynchronously coupled to the ice dynamics with a 100 year time step. For the coupled dynamics (but not for the RSL calculation), an eustatic approximation is assumed for the marine component of surface loading. Initial surface elevation during the Eemian start of model runs has been recursively adjusted on the basis of best fit models to ensure a close match to present-day topography at completion of the model runs. Glaciation across Nares Strait (between Greenland and Ellesmere Island) is provided for by the inclusion of a truncated northwestern Greenland ice sheet.

[15] We postprocess relative sea level histories for model results using the gravitationally self-consistent theory most recently reviewed in detail by *Peltier* [1998]. The RSL tuned model GrB [*Tarasov and Peltier*, 2002] provides the Greenland component of the load history and ICE-4G [*Peltier*, 1994] is used to provide the remaining load histories (i.e., aside from that for North America). The RSL computation takes into account the full load history back to the previous Eemian interglacial, 122 ka ago. Details are provided by *Tarasov and Peltier* [2004].

2.4. Climate and Margin Forcing

[16] The largest source of uncertainty in reconstructing past ice sheet and bed thermal evolution is the continuing lack of a well-constrained climate history. Given current computational resources, the climate forcing chronology is based on an interpolation between observed present-day and LGM climate fields over North America derived from a composite of the PMIP archived −21 ka simulations (http://www-lsce.cea.fr/pmip/index.html). Seven ensemble parameters determine the actual composition of this −21 ka climate as a function of the individual PMIP simulations (Table 2 lists the number of ensemble parameters employed to span the space of plausible glacial systems model behavior). The interpolation is weighted according to a glacial index derived from an inferred regional temperature history for the Greenland summit region [*Tarasov and Peltier*, 2003]. Surface temperature is adjusted to contemporaneous elevation through a lapse rate that varies between 7.5°C km for present-day and 6.0°C km for full glacial conditions. Though these values for the surface temperature lapse rate are close to median for glaciological modeling, it should be noted that recent field studies of Ellesmere Island have found much weaker (order 4°C km) lapse rates [*Marshall et al.*, 2006]. Assuming glacial conditions are analogous to expanded polar climate, these observations along with past analyses from general circulation modeling [*Krinner and Genthon*, 1999] are the motivation for the imposed glacial reduction in surface temperature lapse rate. The present-day temperature climatology is derived from a 14 year mean (1982–1995) of reanalyzed 2 m monthly mean temperature fields [*Kalnay et al.*, 1996]. The present-day precipitation climatology [*Legates and Willmott*, 1990] has been modified to account for evaporative fluxes. There are 13 other ensemble parameters that determine the strength of regional elevation dependencies for precipitation, as well as the exponential phasing of precipitation changes as a function of the glacial index.

[17] The geographic intricacy of the geologically reconstructed ice margin evolution [*Dyke et al.*, 2003; *Dyke*, 2004] is beyond the reach of a freely evolving three-dimensional dynamical ice sheet model that is subject to a simplified climate forcing. As such, this critical constraint is directly enforced. This is accomplished via bounded perturbations to the surface mass balance as required to maintain agreement with the ^{14}C controlled deglacial ice margin chronology [using the INTCAL04 ^{14}C to calendar year conversion of *Reimer et al.* [2004] within the uncertainties of an 80–120 km buffer zone at the margin. This margin forcing is subject to two ensemble parameters controlling the timing of the onset of margin forcing, the interpolation of the margin chronology between time slices, and the width of the margin buffer. Furthermore, the model calibration penalizes this forcing on the basis of the extent of mass balance modifications required.

2.5. Mass Balance and Meltwater Drainage

[18] Surface mass balance is computed with the combination of a positive degree-day model (with temperature-dependent degree-day coefficients) and a physically based refreezing model. A normal statistical model provides the hourly distribution of air temperatures around a monthly mean. Marine ice calving is based on proximity to flotation and also takes into account mean summer sea surface temperature. Lacustrine ice calving and refreezing take into account the available heat capacity of the associated proglacial lake. Given the complexities of the ice-calving process, the ice calving components absorb 4 ensembles parameters. Surface meltwater drainage and lake storage are

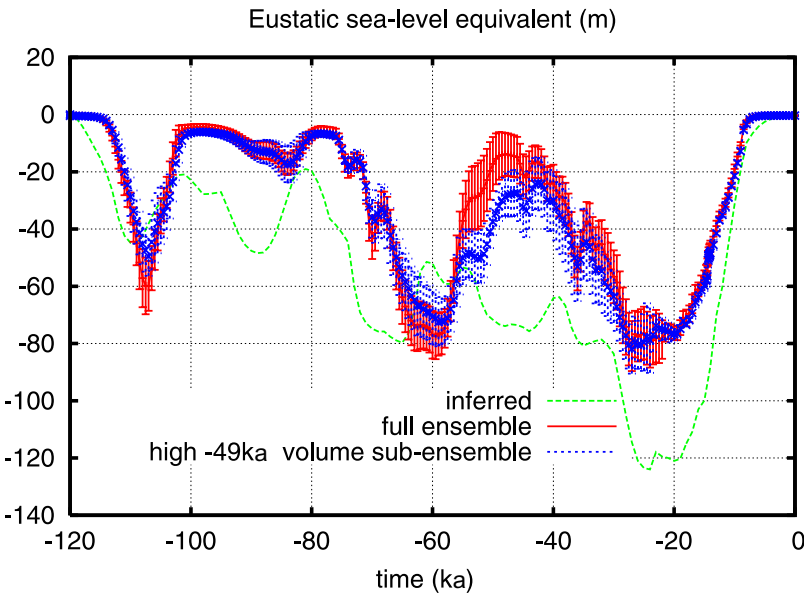

Figure 1. Eustatic sea level chronologies. The inferred global chronology is a blend of chronologies from *Waelbroeck et al.* [2002] and *Peltier and Fairbanks* [2006]. Ensemble results are only for contributions from North America. One sigma confidence intervals indicated are based on fit to constraint data.

accurately computed using a downgradient diagnostic algorithm [*Tarasov and Peltier*, 2005, 2006]. Ground surface temperatures for grid cells that are lake covered are not allowed to descend below 0°C. A simplified heat transfer model is used for thin ice over freshwater lakes.

2.6. Model Calibration

[19] The 32 ensemble parameters currently employed for the GSM (Table 2) are calibrated with a Bayesian methodology (L. Tarasov et al., Bayesian calibration of a glacial systems model of intermediate computational complexity, manuscript in preparation, 2007) against a large constraint data set. The bulk of constraints comprise a large database of paleo-RSL observations (A. S. Dyke, personal communication, 2004) along with geodetic observations for key regions that were never inundated by the sea (and therefore for which there are no RSL observations). Additional calibration constraints include maximum strandline observations south of James Bay and dated strandlines for glacial Lake Agassiz. The calibrated results are further scored according to the fit to a marine limit database [*Dyke et al.*, 2005].

[20] The calibration process involves a 3 step cycle. First, an ensemble of 300–500 runs with the full GSM is computed. The cumulative set of ensemble results is then used to train a set of Bayesian neural networks that emulate the GSM response to ensemble parameters. These neural networks are in turn used to provide the order 1 million run sampling required by Markov Chain Monte Carlo (MCMC) methods. After convergence, the MCMC algorithm samples from the posterior distribution of predicted model fits to the calibration data set as computed by the neural networks. A sampling of the converged MCMC results in turn provides a new set of higher-probability ensemble parameters which are in turn fed into the full GSM to generate a new ensemble.

[21] The ongoing model calibration uses a lower-resolution bed thermal model, and does not archive all the fields required for the present analysis. As such, a 30 member high-probability subensemble has been selected from the ongoing model calibration and rerun with the higher-resolution version of the bed thermal model.

3. Results and Analyses

[22] Model runs are initiated with Eemian boundary conditions 122 ka before present assuming bed thermodynamic equilibrium. All model runs cover a full glacial cycle. Prior to this work, the model calibration had focused on the interval from LGM (about −20 ka) to present. As such, the only constraint prior to LGM was reasonable ice volume bounds at −30 ka [e.g., *Peltier and Fairbanks* 2006]. Analysis in the context of bed thermodynamics has however brought attention to the full cycle of glacial evolution. The only clearly defined constraint prior to LGM is eustatic sea level contributions no more than the inferred eustatic sea level and within 45 m of that value as a maximal contribution from the remaining ice sheets. This constraint however appears to be broken during the −63 to −41 ka interval (Figure 1). Considering the changing phase relationship in Figure 1, the failure of this constraint may largely be due to the phase displacement between the sea level chronology and the climate forcing time dependence which is ultimately derived from the GRIP δ^{18}O chronology. As a bound, a 6 member subensemble with the highest ice volumes at −49 ka was also selected for comparison. However, even this subensemble only weakly meets the constraint within its one sigma confidence interval. The derived North American eustatic sea level contribution (Figure 1) is much

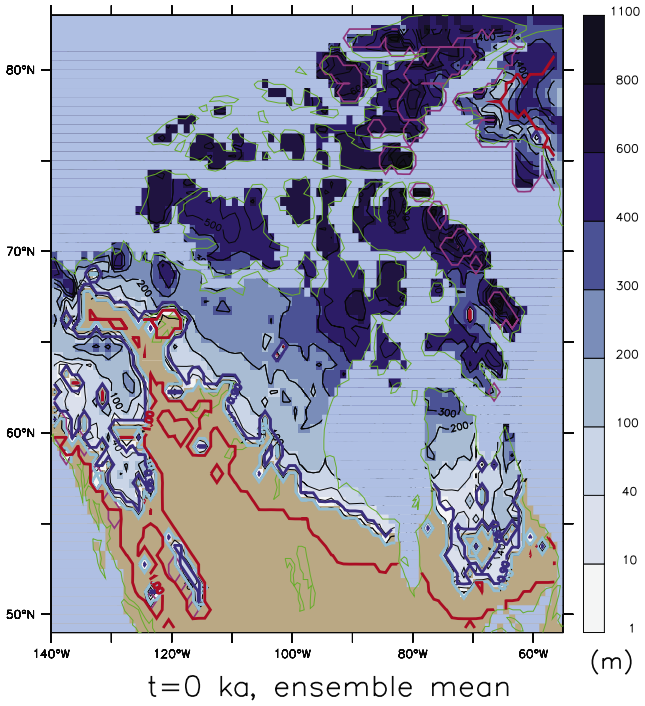

Figure 2. Ensemble mean permafrost depth for present day. Ice margins are shown in mauve; 10% and 90% probable ensemble permafrost extents are indicated by the light and dark blue contours, respectively. Ensemble mean permafrost extent for runs not using TTOP corrections for ground skin temperature is shown in red.

more dynamic than previous studies have suggested [*Tarasov and Peltier*, 1999; *Marshall et al.*, 2000; *Marshall and Clark*, 2002] on account of the strong ice calving and fast flow dynamics selected by the calibration in order to best fit the constraint data. In contrast, without fast flows, the higher volume and thicker ice sheets of *Marshall and Clark* [2002] would have tended to self-stabilize during midglacial warm intervals.

3.1. Present-Day Permafrost Field

[23] Ensemble mean permafrost depth (of lower boundary) ranges to over a kilometer in the high Arctic (Figure 2), with a general increase with latitude. However, the mean permafrost thickness displays strong localized variations, especially in the middle to high Arctic because of surface topography, past submergence, and ice cover history. The detailed structure suggests that observations could be used to test and further constrain the model. The one sigma ensemble range for permafrost depth is generally less than 5% on the continent and less than 10% in the Arctic archipelago, with a few localized exceptions to the west of the Mackenzie delta and Hudson Bay lowlands (plots and/or data are available upon request from the corresponding author).

[24] The ensemble permafrost extent is in general accord with the Permafrost Map of Canada [*Geological Survey of Canada*, 1995] with some excess over Quebec and Labrador and inadequate extent over the northwest sector. These regional discrepancies are likely due to a combination of errors in the temperature climatology, varying snow climatologies, and the thermodynamic impact of varying ground cover and ground composition. The limited extent of these discrepancies is encouraging, especially given the relative simplicity of the permafrost model and the uncertainties associated with ground properties (due to regional variations in heat capacity, thermal conductivity, and porosity). The lack of accounting for mineral versus organic soils alone corresponds to a ±3°C uncertainty in the climatological isotherm at the permafrost boundary. The large overextent of permafrost for the non-TTOP model (red contour in Figure 2) indicates that the TTOP ground surface temperature corrections are essential for reproducing permafrost areal extent.

[25] Another issue of interest is the extent of disequilibrium in the present-day permafrost field. As observed, marginal regions in the ensemble are undergoing retreat (Figure 3). This also holds for islands in the western Arctic that underwent early deglaciation as well as most of Alaska which was largely ice free throughout the whole glacial interval. However, especially in the central Arctic, the permafrost lower boundary depth is as much as 250 m less than the equilibrium value. With the warming that is presently taking place over the Arctic, it appears that there will develop a large region with simultaneous surface thawing and deepening of the permafrost lower boundary.

3.2. Borehole Temperature Profile Comparisons

[26] Comparisons of computed and observed deep borehole profiles offer a time integrated test of the modeling. The temperature profile for Balmertown (Figure 4) is within

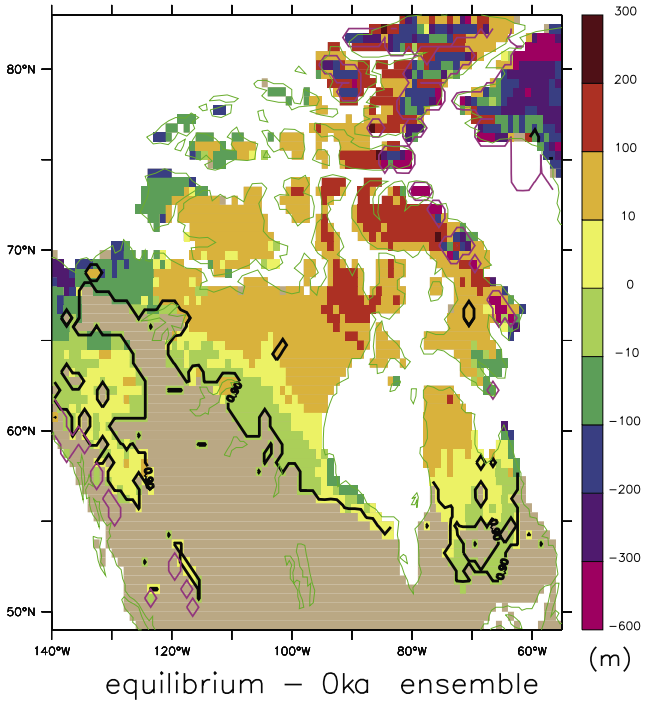

Figure 3. Difference in permafrost depth between equilibrium permafrost computed with present-day climate forcing and that of the ensemble mean. Ice margins are shown in mauve; 90% probable ensemble permafrost extent is shown in black.

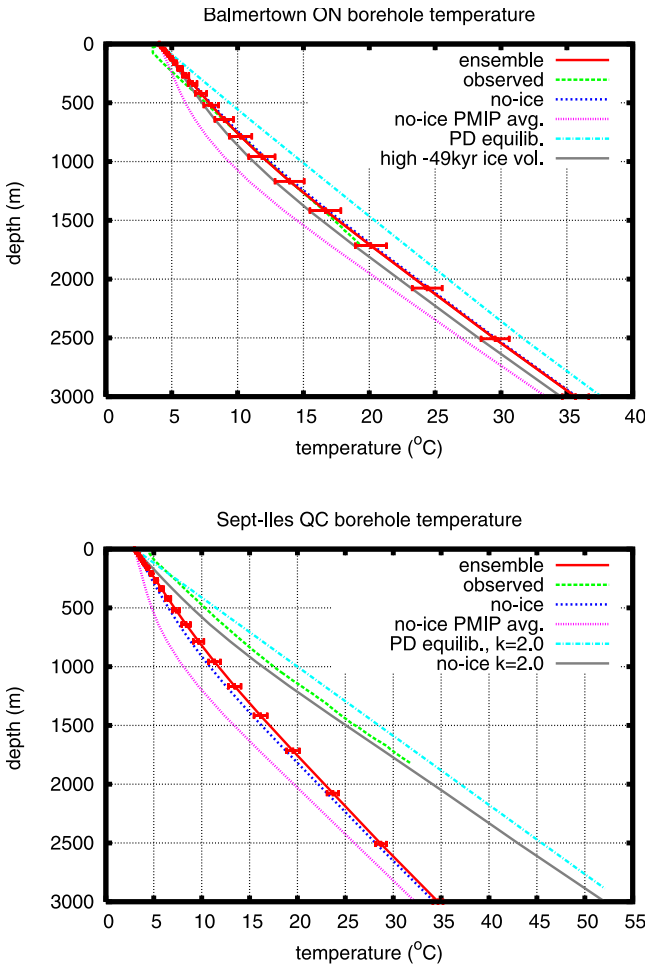

Figure 4. Bed temperature profile comparison for Balmertown (93.7167°W, 51.0333°N) [*Rolandone et al.*, 2003b] and Sept-Iles (6.638°W, 50.213°N) [*Mareschal et al.*, 1999]. The "no-ice" result is from a model run without coupling to the ice sheet model employing the weighted mean values for ensemble parameters. The "no-ice PMIP avg." result employed the raw average of PMIP GCM results for the LGM climate state. "PD equilib." results are equilibrium results with present-day climate forcing; "k = 2" employs a 2.0 W m^{-1} K^{-1} bed thermal conductivity. The "high −49 ka ice vol." result is for the subensemble that better fits the midglacial sea level records as discussed in the beginning of the results and analyses section of the text. Deep geothermal heat fluxes for the covering grid cells are taken from *Rolandone et al.* [2003a].

ensemble error bars except near the surface. The borehole temperature profile is significantly different from an equilibrium profile even down to 3 km. The impact of past ice and climate evolution is therefore well evident in the record.

[27] The temperature profile for an ice-free run (i.e., without the ice sheet model) forced with mean PMIP climate fields (subject to the glacial index weighting over time) is clearly distinct from that observed and from the ensemble weighted mean. However, an ice-free run with the constraint data fit weighted ensemble climate parameters ("no-ice" in Figure 4) has a temperature profile virtually identical to that of the ensemble weighted average. This pattern also holds for the other 3 borehole profiles considered (Figures 4 and 5). As such, it appears that the ice thermodynamics largely cancels the impact of ice surface temperature changes due to elevation changes. This cancellation does not hold at higher latitudes where the permafrost depth over time is significantly larger for ice-free runs. The large misfit of no-ice runs with average PMIP fields compared to no-ice runs with the calibrated climate forcing arguably further validates the significance and quality of the model calibration. This is especially noteworthy as the calibration lacks direct temperature constraints.

[28] The high −49 ka ice volume subensemble has a temperature profile that is colder than that observed (Figure 4). The increased thermal insulation from the extra ice is therefore more than offset by the decreased temperatures required to increase ice extent. This less satisfactory fit compared to that of the full ensemble is not surprising given that this extra constraint was imposed a posteriori to the calibration. The motivation for this subensemble was the

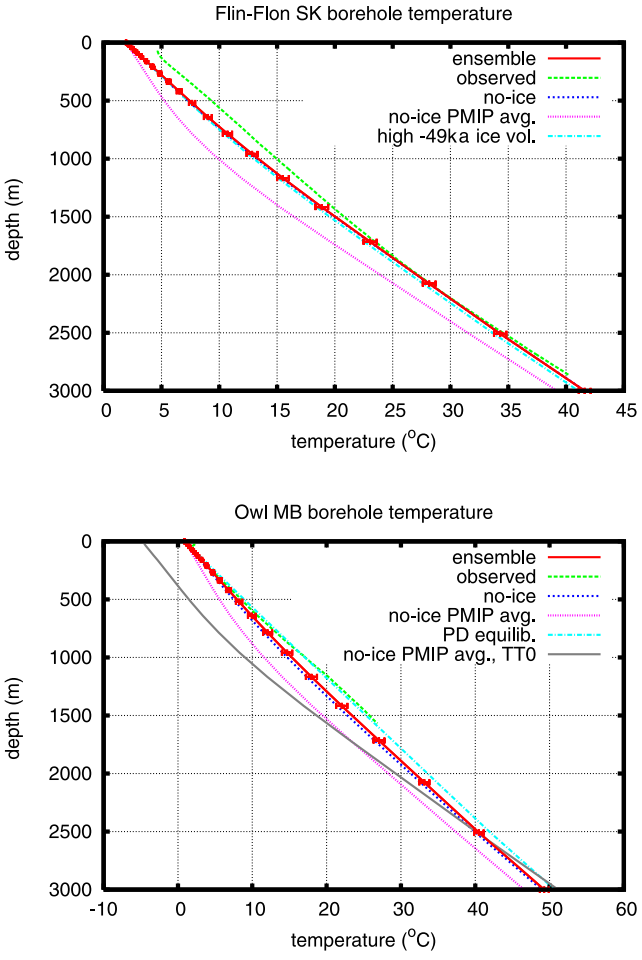

Figure 5. Bed temperature profile comparison for Flin-Flon (102.0°W, 54.717°N) (J. C. Mareschal, personal communication, 2006) and Owl (97.86°W, 55.67°N) [*Rolandone et al.*, 2002]. The "no-ice PMIP avg., TT0" is from a model run identical to the "no-ice PMIP avg." run except for the lack of TTOP ground temperature corrections. Remaining data descriptions are as per Figure 4.

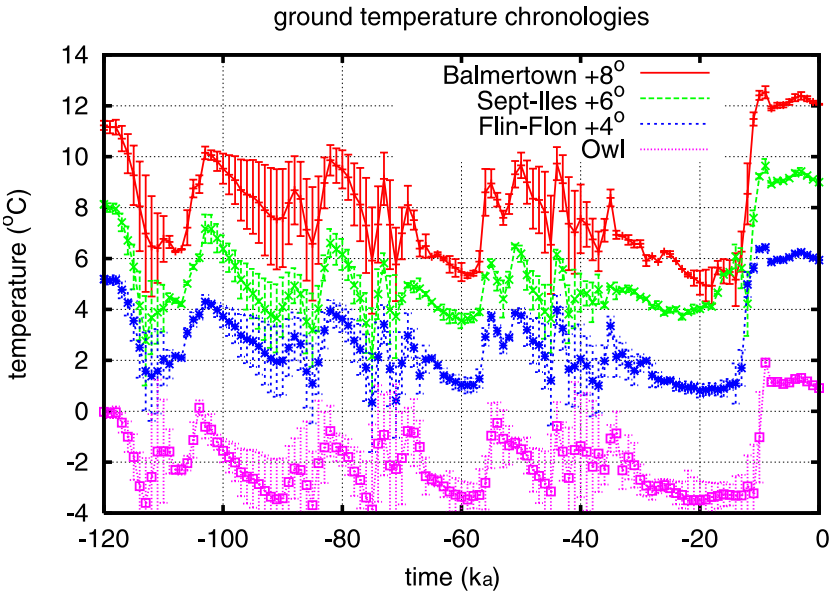

Figure 6. TTOP adjusted ensemble ground temperature chronologies for the four borehole sites.

eustatic sea level misfit around −49 ka of the full ensemble. The weaker fit to the borehole temperature profile of this subensemble further supports the hypothesis that the eustatic sea level misfit of the full ensemble during this time is actually due to a phase displacement between the GRIP δ^{18}O record (from which the climate forcing chronology was indirectly derived) and the eustatic sea level chronology of *Waelbroeck et al.* [2002]. Further investigation is needed to discern the extent to which errors in the GRIP and sea level chronologies contribute, and to which the problem lies with the key assumption that the GRIP δ^{18}O record provides a reasonable reflection of upstream North American climate change.

[29] There is a very large discrepancy between ensemble results and observations for the Sept-Iles borehole (Figure 4). This is due to a thermal conductivity profile of the borehole that is quite different than the homogeneous 3.0 W m^{-1} K^{-1} assumed in the model. A no-ice run with weighted mean ensemble climate parameters employing the observed 2.0 W m^{-1} K^{-1} mean bedrock thermal conductivity [*Rolandone et al.*, 2003a] provides a profile that is quite close to that observed, with a residual discrepancy close to the difference between the k = 3.0 W m^{-1} K^{-1} no-ice and full ensemble profiles, especially below 1 km depth. This suggests that results from an ensemble with the correct bed thermal conductivity would fit the observations. The misfit due to the inappropriate thermal conductivity is much larger than that due to uncertainties in the climate forcing and ice chronology (going by the difference between the profile for the ice-free run with average PMIP climate forcing and that of the calibrated ensemble in Figure 4). This strong sensitivity of the computed borehole temperature profile to the thermal conductivity emphasizes the importance of accurate bed thermal parameters. It also places a caveat on the results obtained in this study, given the use of a single global value for the bed thermal conductivity.

[30] Ensemble borehole temperature profiles for Flin-Flon and Owl (Figure 5), are respectively in agreement only below 1500 m and above 600 m. The misfit for the owl site is within 2 standard deviations. The misfit for the upper half of the Flin-Flon profile is however significant and is likely in large part due to the strong vertical variation in the observed bedrock thermal conductivity for this region [*Rolandone et al.*, 2003a]. The high −49 ka ice volume subensemble provides a virtually identical borehole temperature profile for Flin-Flon to that of the full ensemble, indicating some robustness for this generated temperature profile.

[31] The observed temperature profile for the Owl site (Figure 5) appears to match that of the present-day equilibrium model run. The large difference between the profile for the ice-free model run without the TTOP ground temperature corrections ("TT0", this site is sediment free, so there is no latent heat contribution), supports the importance of using the TTOP corrections in order to obtain valid bed thermal profiles.

[32] The overall (arguably) close fits of the ensemble temperature profiles to observations for three of the boreholes (once appropriate bed thermal conductivities are employed) offers an opportunity to test past inverse modeling of surface temperature chronologies for these sites. *Rolandone et al.* [2003a] have inverted the temperature profiles for the four sites to determine ground surface temperature histories. Their derived chronologies have the peculiar feature of being above 0°C throughout the glacial period for all but the Sept-Iles site. There is thus a clear misfit with our forward modeling for the Flin-Flon, Owl, and Balmertown sites during the −40 to −12 ka interval (Figure 6). The direct modeling of *Sass et al.* [1971] also found that LGM ground surface temperature for Flin-Flon could not have been below 2°C. Above zero ground surface temperatures are inconsistent with ice cover and are therefore inconsistent with current interpretations of regional ice extent during the late glacial period. On the other hand, within the coarse temporal resolution of the inversion, our

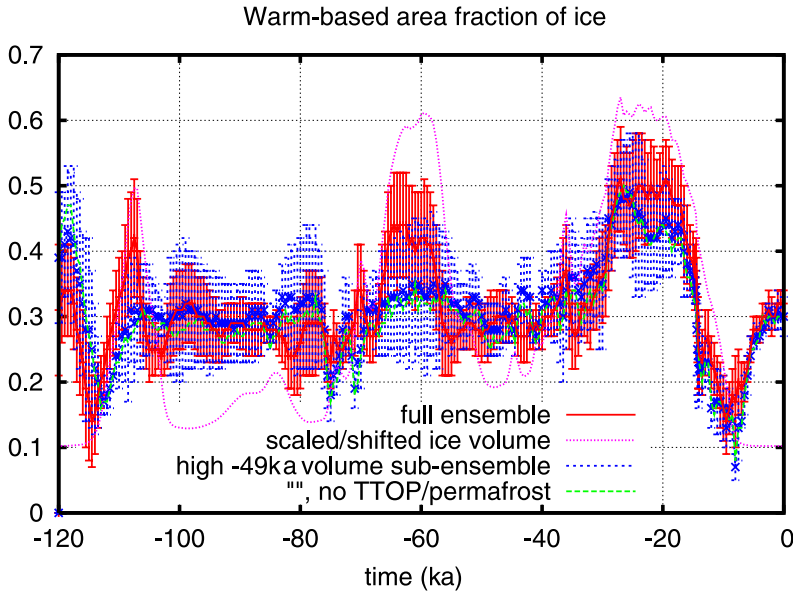

Figure 7. Fractional area chronology of warm-based ice using the −0.2°C (relative to the pressure melting point) ground skin temperature isotherm as a cutoff. Chronologies for the high −49 ka volume subensemble are shown for ensembles run both with and without the TTOP and permafrost components of the bed thermal module. Also shown for direct comparison is a scaled and shifted version of the mean ensemble ice volume chronology.

results approximately match the temperature chronology of *Rolandone et al.* [2003a] for the Sept-Iles site.

3.3. Glacial Era Thermal Characteristics

[33] The ensemble fractional area chronology of warm-based ice (Figure 7) mirrors the dynamic nature of the ice volume chronology (light blue line). The response is more muted for the high −49 ka ice volume subensemble. The warm-based fraction oscillates around 30% until −40 ka with a strong midglacial excursion just before −60 ka. It then climbs to a maximum value of 50% ± 6% at LGM. This is significantly more than the 20–40% range obtained by *Marshall and Clark* [2002] at LGM. It is also much less than the maximum 80–90% range *Marshall and Clark* [2002] obtained by −8 ka. Their result however partially overlaps with the 44% ± 8% LGM range of the high −49 ka ice volume subensemble at LGM.

[34] The delay in the peak warm-based fraction until after LGM in the modeling of *Marshall and Clark* [2002] does not occur in our calibrated modeling. Instead, the three largest peaks for both ice volume and warm-based fraction are well correlated with no discernible phase lag (Figure 7). This is likely due in part to the high ice streaming velocities that the calibration selects. Peak ice velocities of order 10 km/yr are common at the largest ice stream outlets in the better fitting models. This is order 20 times faster than that of *Marshall and Clark* [2002]. Warm-based conditions enable fast flow in the model for regions with present-day sediment cover. The fast flow will initially expand the region of warm-based ice as upstream regions experience ice drawdown with concomitant velocity increases and associated basal warming due to deformation work and basal friction. Over time, high velocities will eventually advect in cold upstream ice and thereby cool the base and thus limit expansion of warm-based regions. Unlike other models, our model controls the timing of large-scale fast flow in Hudson Strait to match the timing of Heinrich events I and II. The Heinrich II event occurs just prior to LGM and thus is well timed to limit the expansion of warm-based ice at LGM.

[35] In contrast to the case of borehole temperature profiles, the impact of the TTOP and permafrost components of the bed thermal model on the warm-based fraction is quite limited as shown for the high −49 ka ice volume subensemble in Figure 7. However, other important aspects such as basal meltwater production are very sensitive to the presence of these components (not shown). In a more advanced glacial systems model that incorporated hydrological controls on fast flow, the impact of a more accurate bed thermal computation on ice sheet (and thereby warm-based fraction) evolution could therefore be significantly higher.

[36] The geographic pattern of warm subglacial conditions at LGM is shown in Figure 8. On the basis of the weighted fits to the constraint data, there is a better than 80% probability that almost all of the south-central and west coast sectors of the ice sheet were warm based at LGM. The south central sector is well know to have had low ice profiles [*Clark*, 1994], and as such the calibration apparently selects model runs with warm temperatures in this region to facilitate fast flow.

[37] The cold-based sector of the Keewatin region (just west of Hudson Bay) matches fairly closely the extent of ribbed moraines and relict landscapes that have been interpreted to be indicators of frozen base conditions at LGM [*Kleman and Hattestrand*, 1999]. However, the cold-based sector in Quebec/Labrador has much less extent than that of the landscape indicators. Below this will be seen to be only partly due to dating uncertainties.

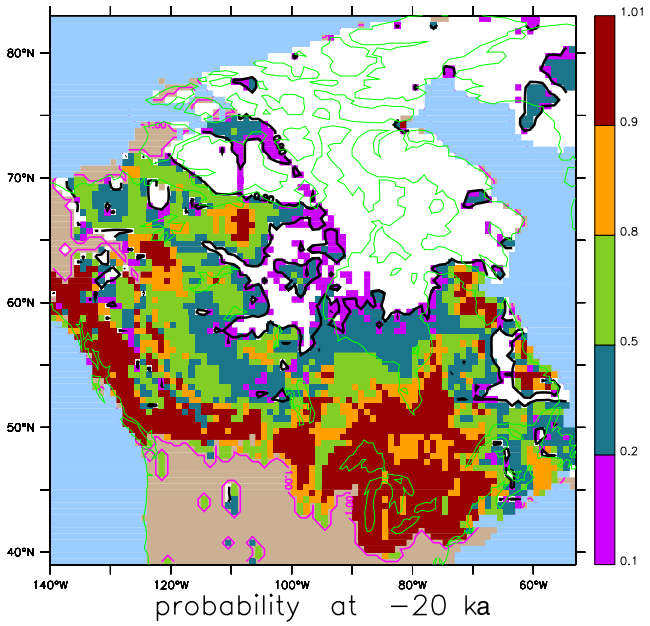

Figure 8. Ensemble probability of subglacial temperature within 0.2°C of the pressure melting point at Last Glacial Maximum (−20 ka). White regions have less than 10% probability; 90% probable ensemble permafrost extents are shown in black. Ice margins are shown in mauve.

[38] In comparison to present day (Figure 9), permafrost was deeper at LGM for (obviously) regions south of the present-day permafrost boundary and for regions that are still occupied by surface ice. On the other hand, the region of the present-day permafrost zone that is currently free of surface ice generally experienced much shallower permafrost at LGM. This further illustrates the strong thermal insulation provided by ice sheets.

[39] This thermal insulative role of ice is even more clearly displayed by comparison of temperature, permafrost, and ice chronologies for specific locations. For both sites in Figure 10, subglacial ground temperature variations are strongly muted in comparison to surface temperature variations. For Balmertown, the mean ensemble ground temperature stays within 5°C of the ground temperature for the "no-ice" run. For the Arctic site, the mean ensemble ground temperature stays within a few degrees of the present-day surface temperature adjusted to the contemporaneous ground surface elevation using the contemporaneous surface temperature lapse rate ("T0(elev)" in Figure 10). Variations in ice thickness also directly affect permafrost depth. This is due to surface load induced changes in the pressure melting point acting via the assumption of hydrostatic pressure throughout the bedrock column.

[40] The continued presence of thick ice for the Arctic site clearly acts to increase the ground surface temperature over time (Figure 10). The abrupt decrease in ground surface temperature following deglaciation provides the main component of the ongoing deglacial thickening of Arctic permafrost (the equilibrium permafrost depth for the Arctic site in Figure 10 is 662 m). The continuing surface temperature cooling for this site provides a smaller but still significant contribution to the present-day disequilibrium in permafrost depth. The close deglacial match between the Arctic site surface air temperature and the purely elevation forced"T0(elev)" temperature in Figure 10 indicates that the change in surface elevation due to postglacial isostatic adjustment is responsible for this continuing postglacial decrease in surface temperature of the Arctic site.

[41] Interpretations of periglacial landforms generally lack strong chronological controls. As such, consideration of the maximum permafrost and warm-based extents since LGM is potentially useful. The 90% probability contour for subglacial permafrost during some part of the last 20 ka (black contour in Figure 11, based on model run fits to the constraint data set) is in closer though still incomplete agreement with that inferred by *Kleman and Hattestrand* [1999] than that for the −20 ka time slice (black contour in Figure 8).

[42] Even more so than for the −20 ka time slice (Figure 8), most regions south of 50°N have a low probability of subglacial cold conditions during the deglacial interval (not shown). Aside from the middle to high Arctic sector, regions that have a low probability of a warm-based subglacial interval during deglaciation are restricted to most of Labrador and central Keewatin (Figure 11). These low-probability to midprobability regions intersect much of ribbed moraine covered sector of Canada. As such, these results suggest that the interpretation of ribbed moraines as indicative of past transition zones between warm and cold-based ice [*Kleman and Hattestrand*, 1999] requires additional controlling factors. The permafrost free west coast

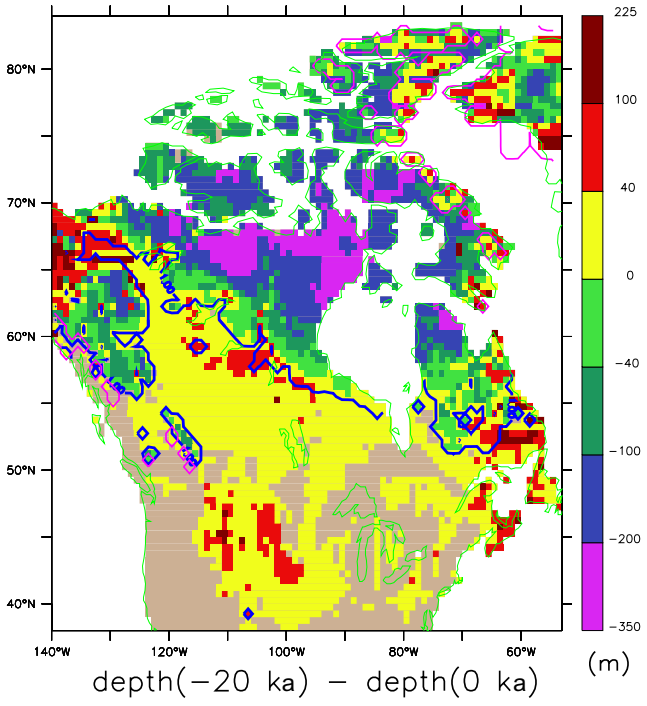

Figure 9. Ensemble mean permafrost depth difference between Last Glacial Maximum (−20 ka) and present. Present-day ensemble mean permafrost extent is indicated by the dark blue contour. Present-day ice margins are shown in mauve.

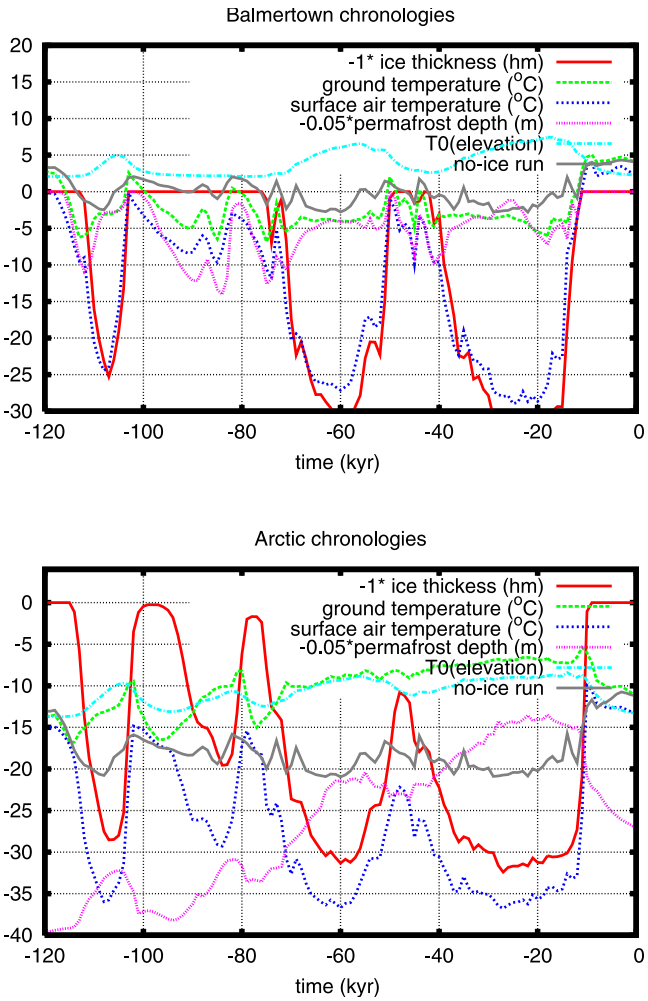

Figure 10. Ensemble ice thickness, mean annual temperature, and permafrost depth chronology for the Balmertown site and for the grid cell at 68.25°N, 91.5°W. The "no-ice" ground temperature result is from a model run without coupling to the ice sheet model employing the weighted mean values for ensemble parameters and constant surface elevation set to present-day values. "T0(elevation)" is the present-day surface air temperature adjusted to the contemporaneous ground surface elevation using the contemporaneous surface temperature lapse rate.

sector in Figure 11 must be interpreted with some caution given the strong subgrid topographic relief in this region.

4. Conclusions

[43] In this paper we have presented a simple set of parameterizations that can significantly improve the accuracy of bed thermal fields under subaerial conditions in relatively coarse resolution large-scale models. Standard large-scale bed thermal models in the glaciology field will otherwise tend to significantly overpredict permafrost extent and underpredict borehole temperature profiles. The current approach is shown to offer a viable low-resolution alternative to dedicated high-resolution permafrost models [e.g., *Zhang et al.*, 2003; *Ling and Zhang*, 2004] when detailed climate forcing fields and land surface parameters are unavailable. However, our work also shows the critical importance of accurate bed thermal parameters. This is exemplified by the large misfit in the original ensemble borehole temperature profile computed for Sept-Iles due to the one third lower bedrock thermal conductivity of the site as compared to the global value used in the model.

[44] Future improvements will include a more accurate deep geothermal heat flux field, more complete and detailed geographic dependence of bed thermal parameters, better (more directly constrained) climate forcings, and explicit and more accurate accounting of the thermodynamic impact of snow cover (the current method accounts for this implicitly on the basis of a regression of Canadian meteorological records). A parameterized thermal offset model for snow that explicitly takes into account the important impact of variations in snow depth seasonality [*Goodrich*, 1982; *Zhang*, 2005] would be most useful in this regard.

[45] We have generated a map of present-day permafrost depth on the basis of calibrated modeling of the last glacial cycle. Though the modeling relies on a simplified climate forcing, with little constraint prior to LGM, the results and to a limited extent the calibration itself have received some regional validation on the basis of a general agreement between observed and modelled temperature profiles for three of four deep boreholes.

[46] In part because of the presence of very fast ice flow/streaming, the evolution of the fraction of warm-based ice does not display the significant phase lag relative to ice volume of a previous study [*Marshall and Clark*, 2002], especially during the last deglaciation. Ensemble results indicate that the maximum warm-based fraction occurred at LGM with a value of 50% ± 6. An average of about 30% was warm based for the early to midglacial interval. The

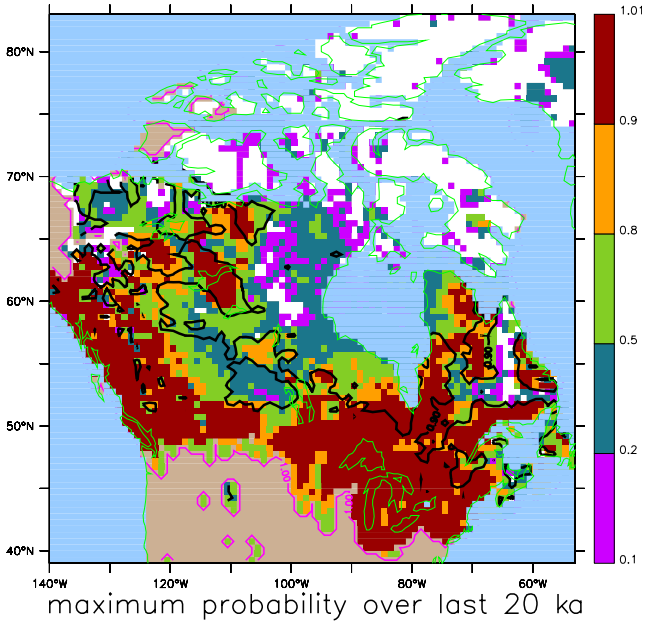

Figure 11. Maximum (ensemble) probability of warm subglacial conditions (basal temperature within 0.2°C of pressure melting point) over the last 20 ka. White regions have less than 10% probability. Maximum 90% probable ensemble permafrost extent is indicated by the black contour.

close correlation between the three largest peaks in both the derived ice volume chronology and the warm-based area fraction suggests that the expansion of warm-based ice played a critical role in the largest glacial advances and retreats.

[47] Analyses also emphasize the strong role that ice sheets play in buffering surface temperatures, with ice thermodynamics approximately cancelling out the strong impact of surface elevation changes on surface temperature. The thermal insulation from the near continuous glacial interval ice cover over the Arctic has resulted in a significant degree of disequilibrium in postglacial permafrost depth that is ongoing. Within most of the present-day ice-free permafrost zone, the depth of the lower permafrost boundary is expected to grow (at least if the local bed thermal conductivity is not significantly above the value of 3.0 W m^{-1} K^{-1} employed in the model). Continuing surface temperature lowering due to changes in surface elevation from postglacial isostatic adjustment has also contributed to this deepening though this is now offset by global warming. This disequilibrium will significantly impact the interpretation of geothermal heat fluxes in and near the permafrost zone. With accurate bed thermal parameters, present-day fields generated by the methodology presented herein can provide initial conditions for more detailed examinations of the future evolution of permafrost and for the inversion of borehole temperature profiles.

[48] **Acknowledgments.** This paper is a contribution to the Polar Climate Stability Research Network that is funded by the Canadian Foundation for Climate and Atmospheric Sciences and a consortium of Canadian universities. Additional support for the work has been provided by NSERC grant A9627. We thank J. C. Mareschal for providing the borehole temperature profiles and review comments. This paper also benefited from a very detailed review by S. J. Marshall.

References

Bauder, A., D. M. Mickelson, and S. J. Marshall (2005), Numerical modeling investigations of the subglacial conditions of the southern Laurentide ice sheet, *Ann. Glaciol.*, *40*, 219–224.

Clark, P. U. (1994), Unstable behaviour of the Laurentide Ice Sheet over deforming sediment and its implications for climate change, *Quat. Res.*, *41*, 19–25.

Dyke, A. S. (2004), An outline of North American deglaciation with emphasis on central and northern Canada, in *Quaternary Glaciations—Extent and Chronology, Part II*, vol. 2b, edited by J. Ehlers and P. L. Gibbard, pp. 373–424, Elsevier, New York.

Dyke, A. S., A. Moore, and L. Robertson (2003), Deglaciation of North America, *Tech. Rep. Open File 1574*, scale 1:7,000000, Geol. Surv. of Can., Ottawa.

Dyke, A. S., L. A. Dredge, and D. A. Hodgson (2005), North American deglacial marine- and lake-limit surfaces, *Geogr. Phys. Quat.*, *59*(2–3), 155–185.

Dziewonski, A. M., and D. L. Anderson (1981), Preliminary reference Earth model, *Phys. Earth Planet. Inter.*, *25*, 297–356.

Geological Survey of Canada (1995), Canada permafrost, *Map 1880A*, Ottawa.

Goodrich, L. E. (1982), The influence of snow cover on the ground thermal regime, *Can. Geotech. J.*, *19*, 421–432.

Kalnay, E., et al. (1996), The NCEP/NCAR 40-year reanalysis project, *Bull. Am. Meteorol. Soc.*, *77*, 437–471.

Kleman, J., and C. Hattestrand (1999), Frozen-bed Fennoscandian and Laurentide ice sheets during the Last Glacial Maximum, *Nature*, *402*(6757), 63–66.

Krinner, G., and C. Genthon (1999), Altitude dependence of the ice sheet surface climate, *Geophys. Res. Lett.*, *26*, 2227–2230.

Laske, G., and G. Masters (1997), A global digital map of sediment thickness, *Eos Trans. AGU*, *78*(46), Fall Meet. Suppl., Abstract S41E-01.

Legates, D. R., and C. J. Willmott (1990), Mean seasonal and spatial variability in gauge-corrected global precipitation, *Int. J. Climatol.*, *10*(2), 111–127.

Licciardi, J. M., P. U. Clark, J. W. Jenson, and D. R. Macayeal (1998), Deglaciation of a soft-bedded Laurentide Ice Sheet, *Quat. Sci. Rev.*, *17*, 427–448.

Ling, F., and T. Zhang (2004), A numerical model for surface energy balance and thermal regime of the active layer and permafrost containing unfrozen water, *Cold Reg. Sci. Technol.*, *38*, 1–15, doi:10.1016/S0165-232X(03)00057-0.

Mareschal, J., F. Rolandone, and G. Bienfait (1999), Heat flow variations in a deep borehole near Sept-Iles, Quebec, Canada: Paleoclimatic interpretation and implications for regional heat flow estimates, *Geophys. Res. Lett.*, *26*, 2049–2052.

Marshall, S. J., and P. U. Clark (2002), Basal temperature evolution of North American ice sheets and implications for the 100-kyr cycle, *Geophys. Res. Lett.*, *29*(24), 2214, doi:10.1029/2002GL015192.

Marshall, S. J., L. Tarasov, G. K. C. Clarke, and W. R. Peltier (2000), Glaciology of Ice Age cycles: Physical processes and modelling challenges, *Can. J. Earth Sci.*, *37*, 769–793.

Marshall, S. J., M. J. Sharp, D. O. Burgess, and F. S. Anslow (2006), Near-surface temperature lapse rates on the Prince of Wales Icefield, Ellesmere Island, Canada. Implications for regional downscaling of temperature, *Int. J. Climatol.*, *27*(23), 385–398.

Mottaghy, D., and V. Rath (2006), Latent heat effects in subsurface heat transport modelling and their impact on palaeotemperature reconstructions, *Geophys. J. Int.*, *164*, 236–245, doi:10.1111/j.1365-246X.2005.02843.x.

Osterkamp, T. E. (1987), Freezing and thawing of soils and permafrost containing unfrozen water or brine, *Water Resour. Res.*, *23*(12), 2279–2285.

Osterkamp, T. E., and J. P. Gosink (1991), Varaiations in permafrost thickness in response to changes in paleoclimate, *J. Geophys. Res.*, *96*, 4423–4434.

Payne, A. J., et al. (2000), Results from the EISMINT model intercomparison: The effects of thermomechanical coupling, *J. Glaciol.*, *46*(153), 227–238.

Peltier, W. R. (1974), The impulse response of a Maxwell Earth, *Rev. Geophys.*, *12*, 649–669.

Peltier, W. R. (1976), Glacial isostatic adjustment II: The inverse problem, *Geophys. J. R. Astron. Soc.*, *46*, 669–706.

Peltier, W. R. (1994), Ice age paleotopography, *Science*, *265*, 195–201.

Peltier, W. R. (1996), Mantle viscosity and ice age ice sheet topography, *Science*, *273*, 1359–1364.

Peltier, W. R. (1998), Postglacial variations in the level of the sea: Implications for climate dynamics and solid-Earth geophysics, *Rev. Geophys.*, *36*, 603–689.

Peltier, W. R. (2004), Global glacial isostatic adjustment and the surface of the ice-age Earth: The ICE-5G (VM2) model and GRACE, *Annu. Rev. Earth Planet. Sci.*, *32*, 111–149.

Peltier, W. R., and F. G. Fairbanks (2006), Global glacial ice volume and Last Glacial Maximum duration from an extended Barbados sea level record, *Quat. Sci. Rev.*, *25*, 3322–3337.

Peltier, W. R., and X. Jiang (1996), Mantle viscosity from the simultaneous inversion of multiple data sets pertaining to postglacial rebound, *Geophys. Res. Lett.*, *23*, 503–506.

Pollack, H. N., S. J. Hurter, and J. R. Johnson (1993), Heat flow from the Earth's interior: Analysis of the global data set, *Rev. Geophys.*, *31*, 267–280.

Reimer, P. J., et al. (2004), IntCal04 terrestrial radiocarbon age calibration, 26–0 ka BP, *Radiocarbon*, *46*, 1029–1058.

Rolandone, F., C. Jaupart, J. C. Mareschal, C. Gariépy, G. Bienfait, C. Carbonne, and R. Lapointe (2002), Surface heat flow, crustal temperatures and mantle heat flow in the Proterozoic Trans-Hudson Orogen, Canadian Shield, *J. Geophys. Res.*, *107*(B12), 2341, doi:10.1029/2001JB000698.

Rolandone, F., J. Mareschal, and C. Jaupart (2003a), Temperatures at the base of the Laurentide Ice Sheet inferred from borehole temperature data, *Geophys. Res. Lett.*, *30*(18), 1944, doi:10.1029/2003GL018046.

Rolandone, F., J. C. Mareschal, C. Jaupart, C. Gosselin, G. Bienfait, and R. Lapointe (2003b), Heat flow in the western Superior Province of the Canadian shield, Heat flow in the western Superior Province of the Canadian shield, *Geophys. Res. Lett.*, *30*(12), 1637, doi:10.1029/2003GL017386.

Romanovsky, V. E., and T. E. Osterkamp (1995), Interannual variations of the thermal regime of the active layer and near-surface permafrost in northern Alaska, *Permafrost Periglacial Processes*, *6*, 313–335.

Sass, J. H., A. H. Lachenbruch, and A. M. Jessop (1971), Uniform heat flow in a deep hole in the Canadian Shield and its paleoclimatic implications, *J. Geophys. Res.*, *76*, 8586–8596.

Smith, M. W., and D. W. Riseborough (2002), Climate and the limits of permafrost: A zonal analysis, *Permafrost Periglacial Processes*, *13*, 1–15.

Tarasov, L., and W. R. Peltier (1999), Impact of thermomechanical ice sheet coupling on a model of the 100 kyr ice age cycle, *J. Geophys. Res.*, *104*, 9517–9545.

Tarasov, L., and W. R. Peltier (2002), Greenland glacial history and local geodynamic consequences, *Geophys. J. Int.*, *150*, 198–229.

Tarasov, L., and W. R. Peltier (2003), Greenland glacial history, borehole constraints, and Eemian extent, *J. Geophys. Res.*, *108*(B3), 2143, doi:10.1029/2001JB001731.

Tarasov, L., and W. R. Peltier (2004), A geophysically constrained large ensemble analysis of the deglacial history of the North American ice sheet complex, *Quat. Sci. Rev.*, *23*, 359–388.

Tarasov, L., and W. R. Peltier (2005), Arctic freshwater forcing of the Younger Dryas cold reversal, *Nature*, *435*, 662–665.

Tarasov, L., and W. R. Peltier (2006), A calibrated deglacial drainage chronology for the North American continent: Evidence of an Arctic trigger for the Younger Dryas, *Quat. Sci. Rev.*, *25*, 659–688.

Waelbroeck, C., L. Labeyrie, E. Michel, J. Duplessy, J. McManus, K. Lambeck, E. Balbon, and M. Labracherie (2002), Sea-level and deep water temperature changes derived from benthic foraminifera isotopic records, *Quat. Sci. Rev.*, *21*, 295–305.

Weast, R. C. (Ed.) (1981), *CRC Handbook of Chemistry and Physics*, CRC Press, Boca Raton, Fla.

Williams, P. J., and M. W. Smith (1989), *The Frozen Earth: Fundamentals of Geocryology*, Alden, Oxford, U. K.

Zhang, T. (2005), Influence of the seasonal snow cover on the ground thermal regime: An overview, *Rev. Geophys.*, *43*, RG4002, doi:10.1029/2004RG000157.

Zhang, Y., W. J. Chen, and J. Cihlar (2003), A process-based model for quantifying the impact of climate change on permafrost thermal regimes, *J. Geophys. Res.*, *108*(D22), 4695, doi:10.1029/2002JD003354.

W. R. Peltier, Department of Physics, University of Toronto, Toronto, ON, Canada M5S-1A7.

L. Tarasov, Department of Physics and Physical Oceanography, Memorial University of Newfoundland, St. John's, NL, Canada A1B 3X7. (lev@physics.mun.ca)